PLOS COMPUTATIONAL BIOLOGY

RESEARCH ARTICLE

Conservation of conformational dynamics across prokaryotic actins

Natalie Ng[1], Handuo Shi[1], Alexandre Colavin[2], Kerwyn Casey Huang[1,2,3,4]*

1 Department of Bioengineering, Stanford University, Stanford, CA, United States of America, **2** Biophysics Program, Stanford University, Stanford, CA, United States of America, **3** Department of Microbiology and Immunology, Stanford University School of Medicine, Stanford, CA, United States of America, **4** Chan Zuckerberg Biohub, San Francisco, CA, United States of America

* kchuang@stanford.edu

OPEN ACCESS

Citation: Ng N, Shi H, Colavin A, Huang KC (2019) Conservation of conformational dynamics across prokaryotic actins. PLoS Comput Biol 15(4): e1006683. https://doi.org/10.1371/journal.pcbi.1006683

Editor: Enrique M. De La Cruz, Yale University, UNITED STATES

Received: March 26, 2018

Accepted: November 30, 2018

Published: April 5, 2019

Data Availability Statement: We have set up a repository for all our data at https://purl.stanford.edu/cm430hn3276 with the Stanford Lane Library. All data are available there.

Funding: Funding was provided by NSF CAREER Award MCB-1149328 (National Science Foundation: www.nsf.gov), the Stanford Center for Systems Biology under Grant P50-GM107615, and the Allen Discovery Center at Stanford on Systems Modeling of Infection (to K.C.H) (Allen Foundation: www.pgaphilanthropies.org); an Agilent Fellowship and a Stanford Interdisciplinary Graduate

Abstract

The actin family of cytoskeletal proteins is essential to the physiology of virtually all archaea, bacteria, and eukaryotes. While X-ray crystallography and electron microscopy have revealed structural homologies among actin-family proteins, these techniques cannot probe molecular-scale conformational dynamics. Here, we use all-atom molecular dynamic simulations to reveal conserved dynamical behaviors in four prokaryotic actin homologs: MreB, FtsA, ParM, and crenactin. We demonstrate that the majority of the conformational dynamics of prokaryotic actins can be explained by treating the four subdomains as rigid bodies. MreB, ParM, and FtsA monomers exhibited nucleotide-dependent dihedral and opening angles, while crenactin monomer dynamics were nucleotide-independent. We further show that the opening angle of ParM is sensitive to a specific interaction between subdomains. Steered molecular dynamics simulations of MreB, FtsA, and crenactin dimers revealed that changes in subunit dihedral angle lead to intersubunit bending or twist, suggesting a conserved mechanism for regulating filament structure. Taken together, our results provide molecular-scale insights into the nucleotide and polymerization dependencies of the structure of prokaryotic actins, suggesting mechanisms for how these structural features are linked to their diverse functions.

Author summary

Simulations are a critical tool for uncovering the molecular mechanisms underlying biological form and function. Here, we use molecular-dynamics simulations to identify common and specific dynamical behaviors in four prokaryotic homologs of actin, a cytoskeletal protein that plays important roles in cellular structure and division in eukaryotes. The four actin homologs have diverse functions including cell division, cell shape maintenance, and DNA segmentation. Dihedral angles and opening angles in monomers of bacterial MreB, FtsA, and ParM were all sensitive to whether the subunit was bound to ATP or ADP, unlike in the archaeal homolog crenactin. In simulations of MreB, FtsA, and crenactin dimers, changes in subunit dihedral angle led to bending or twisting in filaments of these proteins, suggesting a mechanism for regulating the properties of large

Fellowship (to H.S.); and a Stanford Graduate Fellowship and a Gerald J. Lieberman Fellowship (to A.C.). N.N. was supported by the Stanford Bioengineering Research Experience for Undergraduates program. K.C.H. is a Chan Zuckerberg Investigator. All simulations were performed with computer time provided by the Extreme Science and Engineering Discovery Environment (XSEDE), which is supported by National Science Foundation grant number OCI-1053575, with allocation number TG-MCB110056 (to K.C.H.). This work was also supported in part by the National Science Foundation under grant PHYS-1066293 and the hospitality of the Aspen Center for Physics. The funders had no role in study design, data collection and analysis, decision to publish, or preparation of the manuscript.

Competing interests: The authors have declared that no competing interests exist.

filaments. Taken together, our simulations set the stage for understanding and exploiting structure-function relationships of prokaryotic cytoskeletons.

Introduction

The eukaryotic cytoskeleton, which is critical for many cellular functions such as cargo transport and morphogenesis, is comprised of three major elements: actin, tubulin, and intermediate filaments. These proteins bind nucleotides and form highly dynamic polymers [1]. Each of these proteins has numerous homologs across the bacterial and archaeal kingdoms that dictate cell shape and various intracellular behaviors [1, 2]. However, relatively little is known about the structural dynamics of these prokaryotic homologs and whether dynamical behaviors are conserved.

Among bacterial cytoskeletal proteins, actin homologs are the most structurally and functionally diverse class identified thus far. Although sequence homology to eukaryotic actin is generally low, prokaryotic actins have been identified via X-ray crystallography based on their structural homology to eukaryotic actin [3–6], which has a U-shaped four-domain substructure, with two beta domains and a nucleotide binding pocket between two alpha domains [7]. Among the actin homologs, one of the best studied is MreB, which forms filaments that coordinate cell-wall synthesis in many rod-shaped bacteria and is essential for maintaining cell shape in these species [8, 9]. FtsA is an actin homolog with a unique structural domain swap that is essential for anchoring the key cell-division protein and tubulin homolog FtsZ to the membrane [5, 10]. The actin homolog ParM forms filaments that move R1 plasmids to opposite ends of rod-shaped bacteria prior to cytokinesis [11]. Crenactin forms part of the archaeal cytoskeleton [12]; its biological function is currently unknown, but it is hypothesized to be involved in DNA segregation and/or cell-shape control [12]. Given the common structural features of prokaryotic actins, it is unknown how they exert such a wide variety of functions. Features such as the domain swap in FtsA suggest that some proteins may have the capacity for unique intramonomeric conformational changes [13]. Another possibility is that functional differences emerge at the filament level: a wide variety of double-protofilament bacterial-actin filament structures have been observed [14, 15]. The extent to which lessons about structure-function relationships are general across the diverse actin family can be informed by understanding commonalities and distinctions in their structural dynamics.

While X-ray crystallography and cryo-electron microscopy (cryo-EM) have proven critical for elucidating the structures of monomers and filaments of prokaryotic actins, understanding the mechanisms by which these proteins exert their functions, particularly their mechanical roles, requires integration with other experimental and computational techniques. Microscopy has revealed that most actin homologs can form long filaments within cells [3, 4, 16–19]. *In vitro*, ParM filaments exhibit dynamic instability [20], and all actin homologs except FtsA have been observed to undergo nucleotide hydrolysis [12, 21, 22]. However, these experimental techniques lack the spatial and temporal resolution necessary to understand how these filament properties are linked to changes in structure.

Various mechanistic models of cytoskeletal function have focused on nucleotide hydrolysis as a key determinant of filament mechanics [23–25]. Understanding how nucleotide hydrolysis and polymerization affect structural transitions in prokaryotic actins requires a method that can interrogate molecular behaviors with atomic resolution. All-atom molecular dynamics (MD) simulations have been successfully employed to probe the effects of perturbations on prokaryotic and eukaryotic cytoskeletal proteins. MD simulations of eukaryotic actin

monomers have uncovered nucleotide-dependent changes in the structure of the nucleotide-binding pocket [26], and simulations of actin filaments showed nucleotide-dependent changes to filament bending [27]. MD simulations predicted that GTP hydrolysis of the tubulin homolog FtsZ can result in substantial polymer bending [28], which was subsequently verified through X-ray crystallography [29]. MD simulations of MreB and FtsA filaments also revealed intra- and inter-subunit changes with important implications for their respective cellular functions [13, 17]. In sum, structural changes to cytoskeletal filaments are generally observable within the time frame accessible to MD simulations, potentiating a systematic survey of general and specific connections among bound nucleotide, polymerization, and subunit conformations across the prokaryotic actin family.

Here, we used MD simulations to probe the conformational dynamics of monomers and filaments of MreB, FtsA, ParM, and crenactin (Fig 1). We found that these proteins exhibit a wide range of intrasubunit motions that are generally well described by the centers-of-mass of their four subdomains, and hence the majority of monomer dynamics can be explained by changes in opening and dihedral angles formed by the subdomain centers. Our results predict that some proteins exhibit strong dependence on the bound nucleotide, while others are unaffected by hydrolysis. In ParM, opening is inhibited by interactions between two subdomains. As with MreB, changes in the dihedral angle of FtsA and crenactin subunits generally impact the bending or twisting of polymers. This work provides insight into how molecular-scale perturbations of these proteins contribute to their diverse roles in cell-shape regulation and intracellular organization across bacteria and archaea.

Results

The nucleotide-dependent conformational dynamics of MreB are well represented by the centers of four subdomains

In a previous study, we performed all-atom MD simulations on unconstrained MreB monomers using CHARMM27 force fields and found that ATP-bound monomers had larger opening and dihedral angle than ADP-bound monomers [13]. For our study of prokaryotic actins, we first sought to interrogate the robustness of these findings with respect to the force field used and the dimensional reduction to the centers-of-mass of subdomains IA, IB, IIA, and IIB of actin family members.

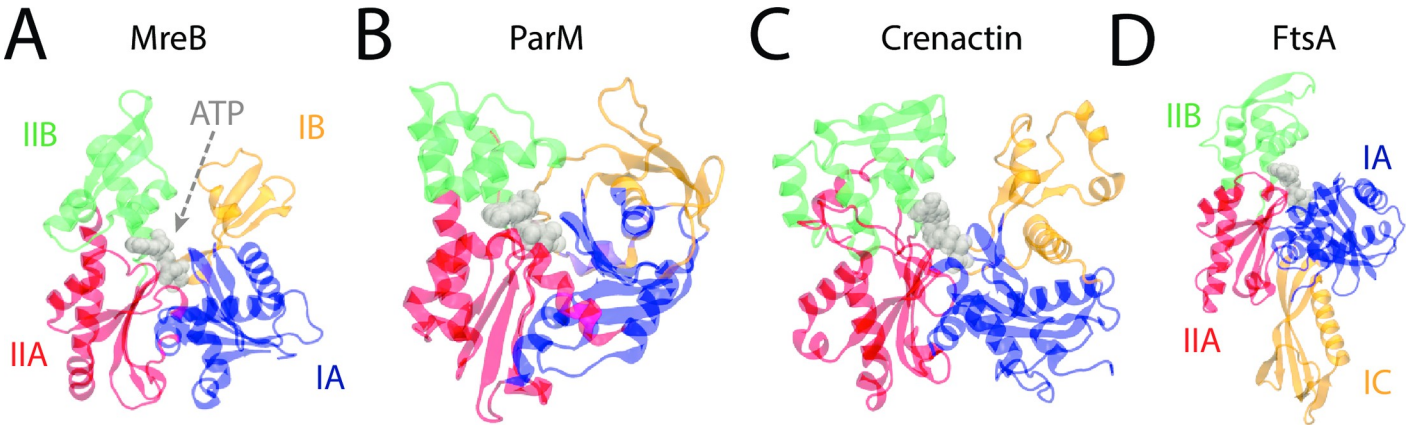

Fig 1. Structures of prokaryotic actin homologs. A-C) The crystal structures of (A) MreB (PDB ID: 1JCG), (B) ParM (PDB ID: 1MWM), and (C) crenactin (PDB ID: 4CJ7) display a characteristic U-shaped actin-like fold described by four subdomains surrounding an enclosed ATP-binding pocket (gray). (D) The crystal structure of FtsA (PDB ID: 4A2B) shows a domain swap of IB to IC.

https://doi.org/10.1371/journal.pcbi.1006683.g001

While simulations using different force fields mostly preserve large-scale motions, distinct behaviors can emerge at finer levels of detail [30]. Thus, we performed all-atom MD simulations on *Thermatoga maritima* MreB (PDB ID: 1JCG) [4] using CHARMM36 force fields [31]. As done previously for actin [32] and MreB [28], we quantified conformational changes by calculating two opening angles (Fig 2A) and a dihedral angle (Fig 2C) from the center of mass of each of the four subdomains (Methods). We carried out all simulations until the opening and dihedral angles adopted distributions that were well fit by Gaussians (we define this state as "equilibrated"), and compared mean values across independent replicate simulations. MreB monomers reached stability within ~55 ns of simulation in our previous study using CHARMM27 force fields [13], and we observed similar time scales using CHARMM36. We extended one MreB-ATP simulation to 80 ns, and the opening angle remained similar (S1A Fig), suggesting the open conformation of MreB is stable on our simulation time scale. While the opening angle was 5–10˚ smaller with CHARMM36 than with CHARMM27 [13] (Figs 2B and S1A), in both sets of simulations subdomains IB and IIB of ATP-bound monomers rapidly hinged apart to form stable, open conformations. Additionally, using CHARMM36, the opening angle stabilized at smaller angles for ADP- than ATP-bound MreB (S1B Fig), as expected from our previous study [13]. ATP-bound MreB monomers also adopted a larger dihedral angle than ADP-bound monomers using CHARMM36, similar to CHARMM27 (Fig 2C and 2D, S1C Fig). Thus, despite small differences, a similar nucleotide dependence in the conformation of MreB monomers was observed using both CHARMM27 and CHARMM36 force fields, supporting our use of CHARMM36 going forward.

While previous studies used the centers-of-mass of the four subdomains of actin-family proteins to dramatically reduce the dimensionality of the protein structure [4, 13, 32], it is also possible for conformational changes to arise within subdomains in addition to the hinges between them. To distinguish between these scenarios, we calculated the root mean square deviation (RMSD) of the C_α atoms from the energetically minimized structure for each subdomain separately, and also for the entire protein, at each time point of our simulations.

In the CHARMM27 ATP-bound simulation, the RMSD of the entire protein increased past 5 Å as the opening angle increased. However, the RMSD of each subdomain remained at ~2 Å (S1D Fig), suggesting that most conformational changes were inter-subdomain. Unsurprisingly, since the CHARMM36 simulation adopted a smaller opening angle than the CHARMM27 simulation, the RMSD of the protein was smaller as well (Fig 2E). Nonetheless, consistent with the CHARMM27 simulation, the RMSD of each subdomain was smaller than the RMSD of the whole protein (Fig 2E). To determine whether subdomain structure was consistent between distinct MreB monomer conformations, we computed RMSDs between the CHARMM36 equilibrium structure and the CHARMM27 simulation at each time point. Since the CHARMM27 simulation adopted a larger opening angle than the CHARMM36 simulation, the RMSD of the whole protein increased relative to the CHARMM36 equilibrium structure. Still, the subdomain RMSDs remained at ~2 Å (S1E Fig). Thus, the structure of each subdomain was largely maintained as the whole protein underwent large conformational changes.

To further quantify the stability of the MreB subdomains, we performed a principal component analysis (PCA) on the simulation trajectory of an ATP-bound MreB. The eigenvector with the largest eigenvalue explained 70.3% of the variance in the whole protein. We then performed PCA on each of the four subdomains separately, and found that the eigenvector with the largest eigenvalue explained only 25.5% to 45.9% of the variance. These results indicate that the trajectory of the protein can be largely explained through global, systematic changes, while the subdomains exhibit more randomness in their motion (S1F Fig). We perturbed the mean MreB structure along the first eigenvector, and identified that movement along the first

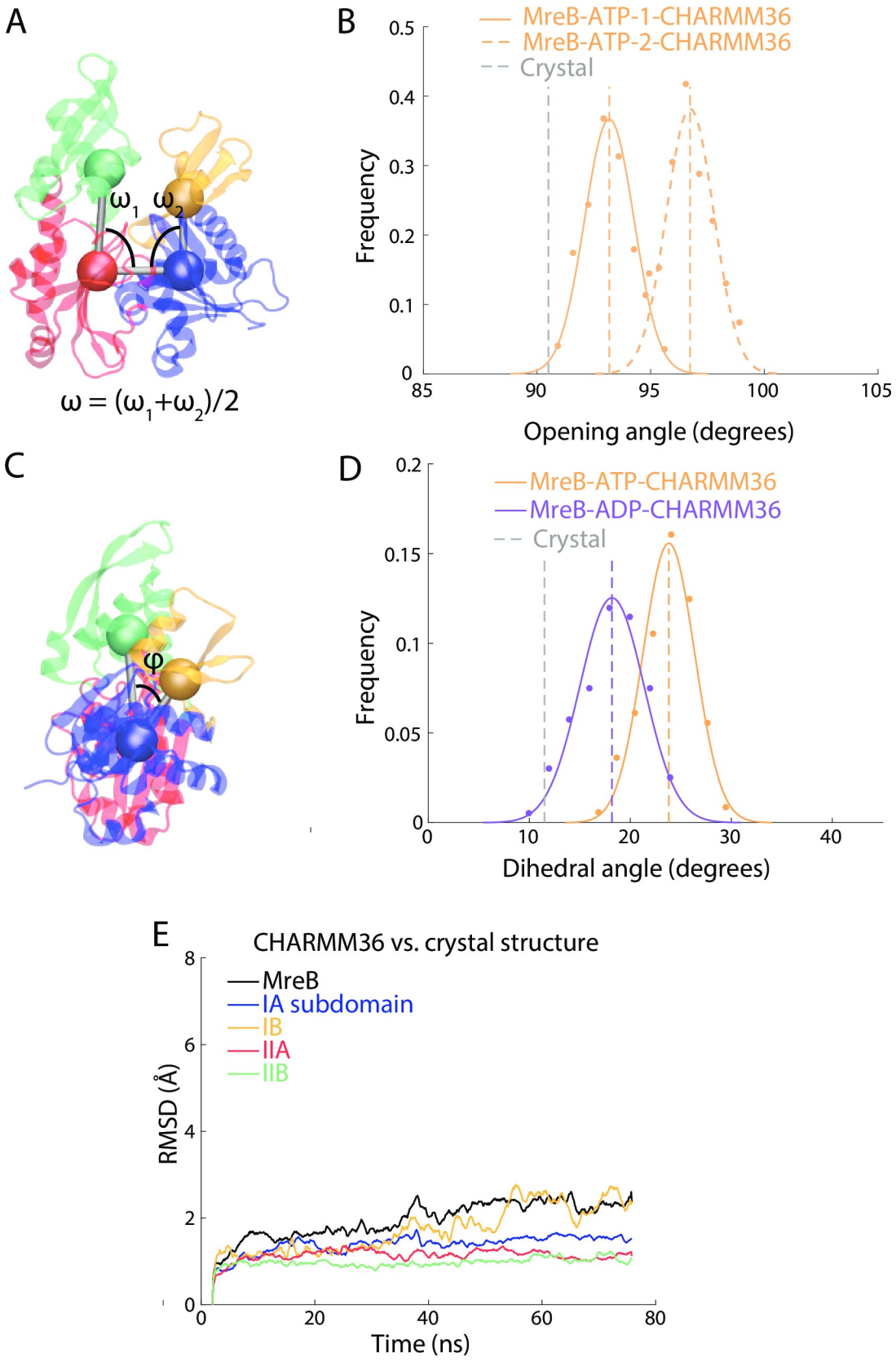
A
ω1
ω2
ω = (ω1+ω2)/2
B
MreB-ATP-1-CHARMM36
MreB-ATP-2-CHARMM36
Crystal
Frequency
Opening angle (degrees)
C
φ
D
MreB-ATP-CHARMM36
MreB-ADP-CHARMM36
Crystal
Frequency
Dihedral angle (degrees)
E
CHARMM36 vs. crystal structure
MreB
IA subdomain
IB
IIA
IIB
RMSD (Å)
Time (ns)

Fig 2. MreB adopts multiple conformations with nucleotide-dependent opening and dihedral angles. (A) The opening angle of an MreB monomer is defined as the average of the internal opening angles. (B) The opening angle distribution in the last 30 ns of simulation for ATP-bound MreB monomers. The opening angle of an ATP-bound MreB monomer stabilized at an even larger value in a CHARMM27 simulation. The rest of the simulations in this manuscript use CHARMM36 force fields, unless otherwise noted. Dashed lines are mean values. Gray dashed line is the value in the crystal structure. (C) Schematic illustrating calculation of the dihedral angle. (D) Histograms of the dihedral angle during the last 30 ns of the simulations show that an ATP-bound MreB monomer adopts a larger dihedral angle than an ADP-bound MreB monomer. Dashed lines are mean values. Gray dashed line is the value in the crystal structure. (E) The RMSD of the entire protein for the CHARMM36 MreB-ATP-1 simulation relative to the initial equilibrated structure remained relatively low compared with (S1D Fig). The RMSDs of the four subdomains remained ~2 Å.

https://doi.org/10.1371/journal.pcbi.1006683.g002

eigenvector corresponds to changes in the opening angle (S1G Fig). To complement these findings, we performed a cross-correlation analysis on MreB using the Bio3D package [33], and showed that subdomains IA/IB exhibited highly correlated, collective motions. The same was true for subdomains IIA/IIB, and the two groupings (IA/IB and IIA/IIB) had opposing movements. These results support our conclusion that the intramonomeric dynamics of MreB can mostly be represented by the relative motions of its subdomains (S1H Fig). Simulations at longer time scales have the potential to reveal dynamics within MreB subdomains and increase our understanding of how intra-subdomain changes fine-tune MreB functions.

FtsA monomers exhibit nucleotide-dependent conformational changes

We next investigated FtsA (PDB ID: 4A2B), an essential protein involved in tethering the key division protein FtsZ to the membrane [5, 10]. FtsA has a four-subdomain architecture similar to those of actin and MreB, but subdomain IB is replaced by a new subdomain (IC) located on the opposite side of subdomain IA (Fig 1) that has no structural similarity to the actin subdomains [5]. To determine whether this domain swap impacts the conformational dynamics around the nucleotide-binding pocket and alters the coupling of dihedral/opening angles to nucleotide hydrolysis, we first carried out all-atom unconstrained MD simulations on ATP- and ADP-bound FtsA monomers.

While FtsA monomers showed little conformational flexibility, they still exhibited distinct ATP- and ADP-bound states with respect to opening and dihedral angles (Fig 3A and 3B, Methods). In all simulations, the RMSD of each subdomain as well as the entire protein remained <2 Å (S2 Fig), and the opening angle exhibited very little variation. Compared to an ATP-bound MreB monomer, whose opening angle reached a different equilibrium value (102.1±2.4˚ and 93.2±1.0˚, mean ± standard deviation (s.d.) measured over the final 30 ns of simulation) in replicate simulations, the opening angle of an ATP-bound FtsA monomer was much more constrained and was highly reproducible (110.1±0.7˚ and 109.6±0.8˚ in two replicates; Fig 3A, 3C and 3D). The FtsA equilibrium opening angle exhibited slight, but highly reproducible, nucleotide dependence: the opening angle for ADP-bound FtsA equilibrated at 112.4±1.0º and 111.5±0.7˚. In ATP- and ADP-bound FtsA, the dihedral angle equilibrated at 20.6±1.9˚ for ATP and 20.3±2.5˚ for ADP, respectively (Fig 3B, 3E and 3F), with a highly reproducible mean value across simulations (Fig 3F).

To address whether the limited duration of our simulations (~200 ns) precluded access to other states of FtsA, we steered the opening angle of an equilibrated ATP-bound monomer up to the equilibrium value in our simulations of an ADP-bound monomer. This conformation was unstable; the opening angle rapidly decreased back to the value in our simulations of an ATP-bound monomer (S3A Fig). Similarly, steering the opening angle of an equilibrated ADP-bound monomer down to the equilibrium value in our simulations of an ATP-bound monomer was followed by rapid re-opening (S3B Fig). Longer time-scale simulations will help to quantify the stability of the ATP- and ADP-bound conformations. Nonetheless, as with

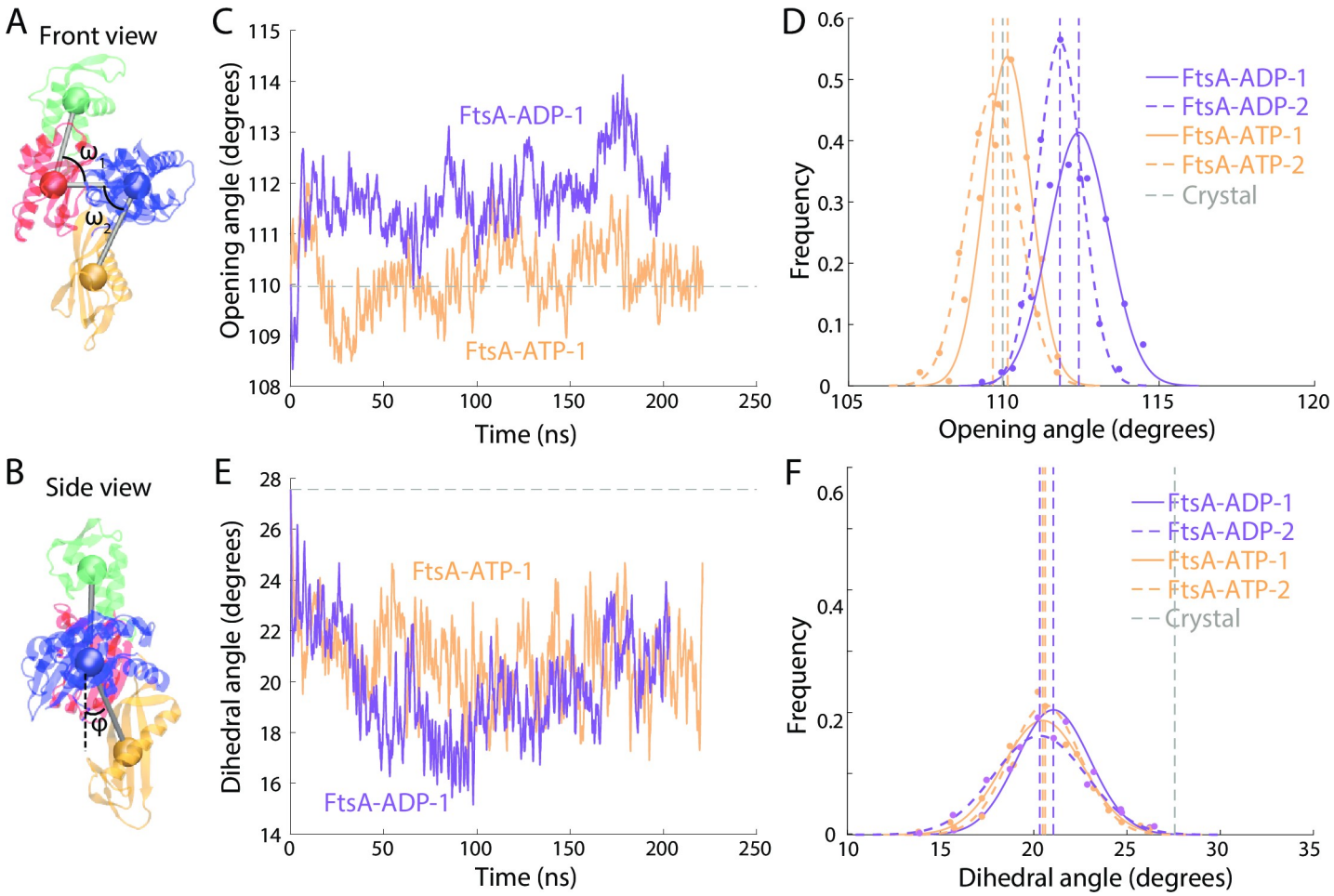

Fig 3. FtsA monomers undergo small but reproducible changes in opening angle upon nucleotide hydrolysis. (A) The domain swap of IB to IC in FtsA necessitated a change in the calculation methodology for opening angle (Methods). (B) Schematic of calculation methodology for FtsA dihedral angle. (C) The opening angle of an ATP-bound FtsA monomer remained centered on the value in the crystal structure (gray dashed line), while an ADP-bound FtsA monomer stabilized at a slightly larger opening angle. (D) The distributions of opening angles over the last 30 ns of simulation were highly reproducible across the two replicate simulations for ATP- and ADP-bound FtsA monomers. Dashed lines are mean values. Gray dashed line is the value in the crystal structure. E,F) The trajectories (E) and distributions (F) of dihedral angles of ATP- and ADP-bound FtsA monomers were similar. Dashed lines are mean values. Gray dashed line is the value in the crystal structure.

https://doi.org/10.1371/journal.pcbi.1006683.g003

MreB and actin, FtsA likely has two distinct states dependent on the bound nucleotide that are stable on the time scale of our simulations.

ParM exhibits high conformational variability with nucleotide-dependent states

We next used all-atom MD simulations to investigate ParM, which forms filaments that push apart plasmids to segregate them into daughter cells [6, 18]. ParM monomers exhibited large, nucleotide-dependent conformational changes, with substantial variability across replicate simulations, suggesting the possibility of multiple conformational states rather than a single equilibrium state. In all simulations of ATP-bound ParM, the opening angle rapidly increased from 97˚ in the crystal structure to over 100˚ (Fig 4A). In one simulation (ParM-ATP-1), subdomains IB and IIB continued to hinge apart to 109.0±2.0˚ after 100 ns, then reverted back to 103.3±2.9˚ in the last 30 ns of the 200-ns simulation (S4A Fig). While this simulation appeared not to converge to a single open state, it potentially revealed the presence of two distinct states

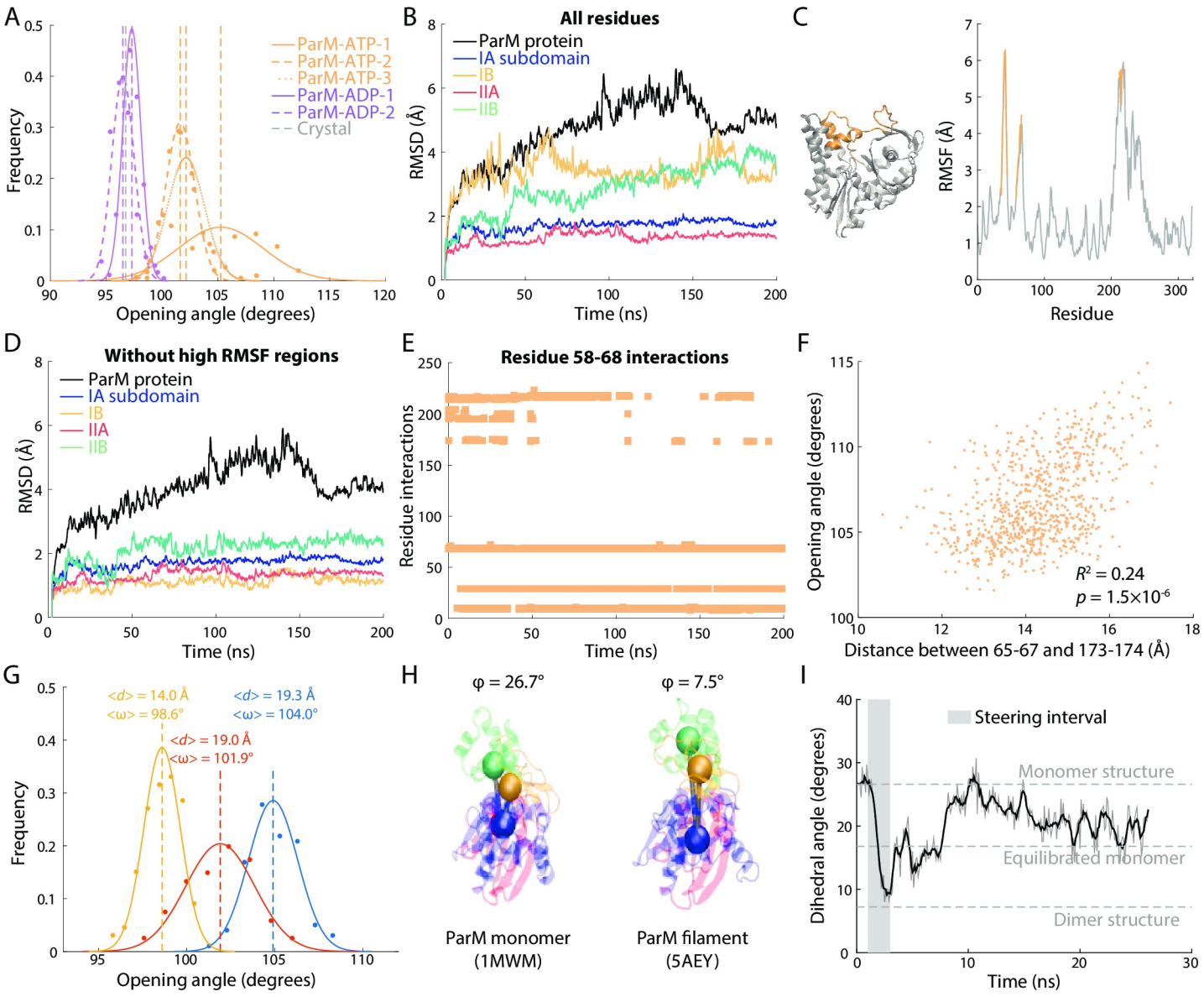

Fig 4. Loop in the IB domain drives ParM monomer opening. (A) The opening angle of ADP-bound ParM monomers remained near the crystal structure value (gray dashed line), while that of ATP-bound ParM monomers consistently increased. Two simulations (ParM-ATP-2,3) consistently exhibited opening angles of ~102˚ after 50 ns and maintained that value, whereas in the other simulation (ParM-ATP-1), the opening angle increased beyond 105˚ after 100 ns and then eventually decreased to ~103˚ in the last 20 ns of the 200-ns simulation (S4A Fig). Dashed lines are mean values. Gray dashed line is the value in the crystal structure. (B) For the ATP-bound ParM simulation in which the opening angle increased beyond 105˚ (ParM-ATP-1), there were large increases in RMSD across the entire protein and in subdomains IIA and IIB. (C) RMSF analysis of single residue fluctuations during the simulation in (B) revealed two regions (residues 58–67 and 173–174, gold) with high RMSF values that were spatially proximal on the crystal structure. (D) For the simulation in (B), when excluding residues 58–67 and 173–174, the RMSDs of all four subdomains dropped to ~2 Å. Thus, these regions were responsible for the conformational variability in (B). (E) Interactions of the loop formed by residues 58–67 with residues 173–174 and 200–202 disappeared early in simulation ParM-ATP-1. Interactions were defined as a minimum distance between residues of <5 Å. (F) The distance (d) between residues 65–67 and 173–174 was highly correlated with the opening angle (ω) across the last 80 ns of the ParM-ATP-1 simulation. The p-value was computed with sampling corresponding to a time interval of 1 ns; for an interval of 3 ns, the p-value is 0.0037. (G) Steering of the distance between residues 65–67 and 173–174 tuned the opening angle in a distance-dependent manner. Dashed lines are mean values. (H) The dihedral angle of a ParM monomer crystal structure (PDB ID: 1MWM) was much higher than that of each subunit in a ParM filament crystal structure (PDB ID: 5AEY). (I) When the dihedral angle of a ParM-ATP monomer was steered to 7.5˚ (gray box) and then released, the angle stabilized at a value similar to unconstrained simulations (S4B Fig), indicating that ParM flattens upon polymerization.

https://doi.org/10.1371/journal.pcbi.1006683.g004

of ATP-bound ParM, both with opening angles larger than the crystal structure. In the other two simulations, the opening angle stabilized at 101.6±1.3˚ and 102.2±1.7˚, but did not further open up. ADP-bound monomers were less open, equilibrating between 97˚ and 99˚ (Fig 4A). Unlike MreB, we did not observe consistent nucleotide dependencies on the dihedral angle of ParM monomers (S4B Fig).

To identify whether certain intrasubunit motions of ParM contributed to the transient period of opening angle >105˚ in our first ATP-bound simulation, we calculated the RMSD of each subdomain and the whole protein relative to the minimized structure in that simulation. Subdomains IB and IIB exhibited large conformational variability, similar to the protein as a whole (Fig 4B). We identified residues 35–45 and residues 58–67 on subdomain IB and residues 211–216 on subdomain IIB as having the greatest root mean square fluctuation (RMSF) (Fig 4C), a measure of the positional variability of specific residues. The subdomain RMSDs calculated after excluding these high-RMSF residues decreased to <2 Å, suggesting a stable core within each subdomain of ParM (Fig 4D). We re-measured opening and dihedral angles excluding these high-RMSF residues, and found that while the overall values changed, the same nucleotide dependencies relating to dihedral and opening angle were observed (S5 Fig).

The high degree of variability in opening angle across replicate simulations suggested the opportunity to identify the structural elements that underlie ParM opening. In the crystal structure, the high RMSF loop of residues 58–67 interacts strongly (defined as a C_α-C_α distance <5 Å) with residues 173–174, which lie near the ATP binding pocket, as well as with residues 200–202 (Fig 4E). In the ParM-ATP-1 simulation with the most variable opening angle, these interactions were largely abolished within 40 ns, but eventually re-established after ~150 ns (Fig 4E). The presence and absence of these interactions largely coincided with the large shifts in opening angle (S4A Fig). Throughout this simulation, the opening angle was highly correlated with the distance between the center of mass of residues 65–67 and the center of mass of 173–174 (Fig 4F). By contrast, in the other two ParM-ATP simulations with smaller opening angles, the interaction between residues 58–67 and 173–174 persisted throughout the simulation (S6A and S6B Fig). In the ParM-ATP-2 simulation, the interaction between residues 58–67 and 173–174 was initially disrupted but quickly recovered (S6A Fig), consistent with the smaller increase in opening angle in this simulation (S4A Fig).

To determine whether disrupting the interaction between residues 173–174 and 58–67 would cause ParM to open, we steered the center-of-mass distance between residues 173–174 and 65–67 from the crystal structure value of 9.3 Å to various larger values. In a steered simulation in which we steered the distance between residues 173–174 and 65–67 to 19.3 Å, the opening angle increased to 104.0±1.4˚ (Fig 4G), suggesting that breaking this interaction directly changes the ParM protein conformation. Steering the distance between residues 173–174 and 65–67 (Fig 4G) to 19.0 Å and 14.0 Å resulted in opening angles of 101.9±2.0˚ and 98.6±1.0˚, respectively, indicating that the distance between residues 173–174 and 65–67 tunes the opening angle of ParM monomers. Longer time-scale simulations, along with more replicates, will be necessary to quantify the frequency of opening-angle transitions, and to determine whether they are always coupled to interactions between the 65–67 and 173–174 residue groups.

The dihedral angles of ParM in a monomer crystal structure [6] and in a cryo-EM filament structure [18] were 26.7˚ and 7.54˚, respectively (Fig 4H), suggesting that polymerization impacts ParM conformations. ParM forms left-handed double-helical filaments that make MD simulations infeasible due to the large number of subunits required to mimic a biologically relevant system. To overcome this challenge and to glean information about whether ParM filaments flatten upon polymerization, we steered the dihedral angle of an ATP-bound ParM monomer to 7˚ to match that of the cryo-EM filament structure. Upon release, the monomer rapidly unflattened to 20˚ (Fig 4I), similar to the stabilized values of our ParM-ATP monomer

simulations (S4B Fig), suggesting that ParM monomers, like MreB [13], flatten upon polymerization. Thus, ParM likely has some similar conformational properties as MreB, even though the interactions between the flexible regions of subdomains IB and IIB unique to ParM provide tunability to its opening angle.

The dihedral angle of prokaryotic actins is coupled to filament bending and twisting

For MreB, we previously discovered that the dihedral angle of the bottom subunit in a dimer simulation was directly coupled to dimer bending [13]. In particular, the intersubunit bending of ATP-bound MreB was correlated to the dihedral angle throughout each simulation, and steering the dihedral angle to a flatter conformation reduced the bending of a dimer structure [13]. We confirmed these findings for the CHARMM36 force field by steering the dihedral angle of the bottom subunit of an MreB-ATP dimer to 23.1˚, 28.3˚, and 33.0˚, and observed the expected inverse relationship between dihedral angle and filament bending (S7 Fig). Given the similarities between the dynamics of MreB and other bacterial actin homologs at the monomeric level, we hypothesized that other actin-like filaments also exhibit intersubunit behaviors coupled to intrasubunit changes.

We performed MD simulations of dimers of FtsA (PDB ID: 4A2B) and *Pyrobaculum calidifontis* crenactin (PDB ID: 4CJ7); crenactin is an archaeal actin homolog for which our MD simulations of ATP- and ADP-bound monomers exhibited similar conformations (S8A and S8B Fig). Dimer structures were initialized from repeated subunits of the appropriate crystal structure. Due to ParM's complicated filament structure, which requires four points of contact per monomer, we were unable to construct biologically relevant ParM dimers with a stable interface *in silico* [34]. For each time step of dimer simulations, we measured two bending angles and one twisting angle between the subunits (Fig 5A and 5D; Methods). We did not observe any significant nucleotide-dependent changes in bending or twisting angles for FtsA and crenactin dimers (S9 Fig), likely because there was little or no nucleotide dependence in monomer conformations of FtsA (Fig 3) and crenactin (S8 Fig), respectively, although it is possible that differences could emerge at longer time scales.

Similar to MreB, the dihedral angle of the bottom subunit of an FtsA dimer was correlated with filament bending along the second bending axis (Fig 5A and 5B). To test whether coupling between the dihedral angle and filament bending was direct, we steered the dihedral angle of the bottom subunit to average values of 16.4˚, 20.8˚, 25.5˚, and 29.6˚ (measured over the last 20 ns of steered simulations; S10A Fig). The resulting bending angles of the dimer shifted systematically with the dihedral angle (Fig 5C), indicating that subunit dihedral changes drive bending of the FtsA filament. Interestingly, the bending angle flipped from positive to negative (Fig 5C); this flexibility could play a key role in regulating the transition of the division machinery from assembly to constriction.

In the crenactin filament crystal structure (PDB: 4CJ7), subunits have a large twisting angle of -47.3˚ (negative indicates a right-handed filament). In our simulations, ATP- and ADP-bound dimers equilibrated between -45˚ and -53˚ (S9D Fig), suggesting that the large twisting angle is not a result of strained crystal contacts. By contrast to MreB and FtsA, the dihedral angle of the bottom subunit of crenactin was not correlated with filament bending, but rather with filament twist (Fig 5D and 5E). To test causality, we steered the dihedral angle of the bottom subunit to 22.6˚, 23.4˚, and 26.7˚ (S10B Fig), and observed progressive increases in twist magnitude (Fig 5F). In sum, coupling of filament degrees of freedom to subunit conformational changes is generalizable across at least some bacterial actin-family members.

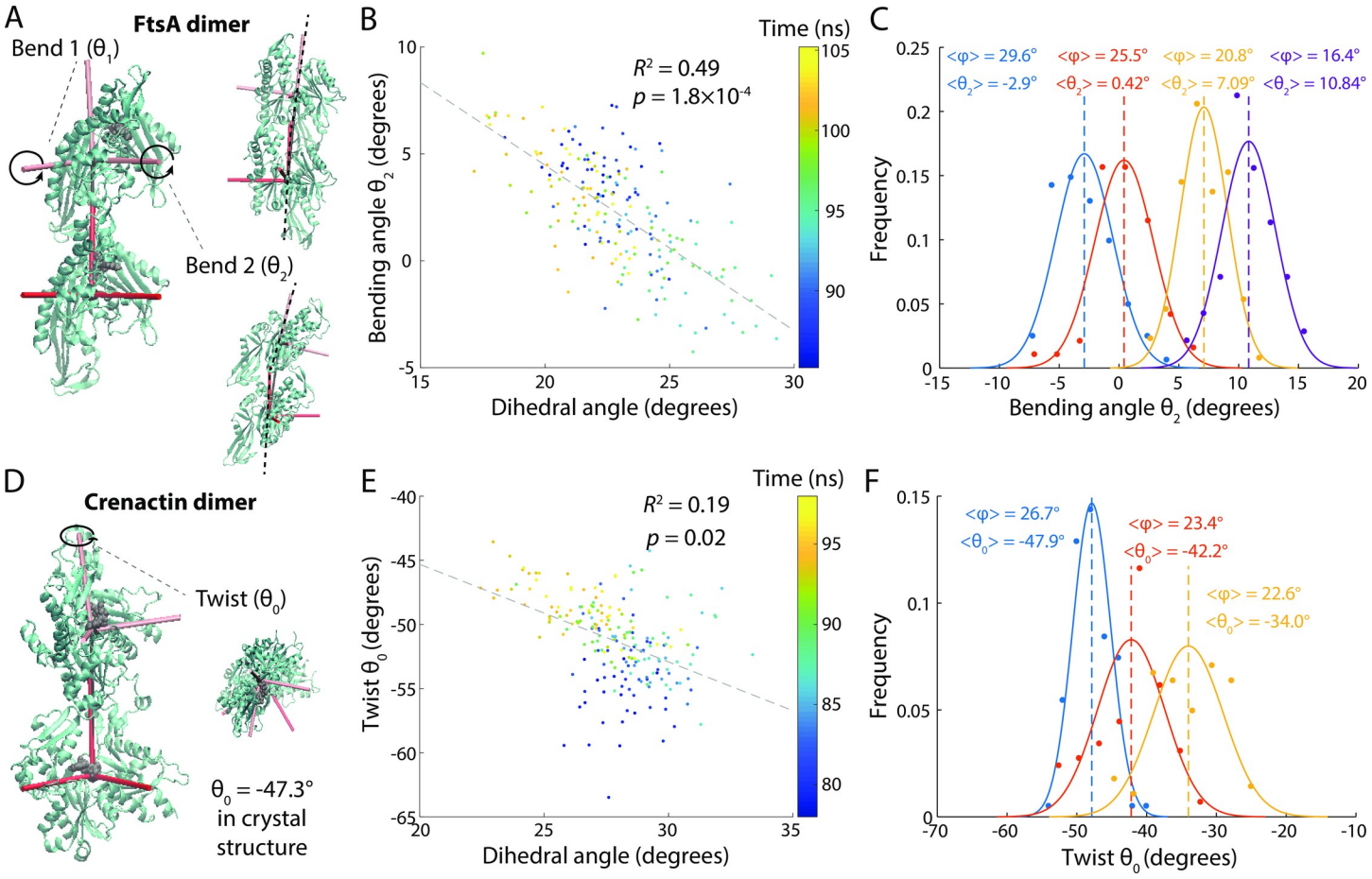

Fig 5. FtsA and crenactin filament bending and twisting are driven by changes to subunit dihedral angles. (A) Illustration of the two possible axes for FtsA dimer bending. (B) The dihedral angle of the bottom subunit in an FtsA-ATP dimer was highly correlated with bending angle θ_2 in all unconstrained simulations. (C) Steering the dihedral angle (φ) of the bottom subunit of an FtsA-ATP dimer from 16.4˚ to 29.6˚ caused systematic shifts in the bending angle θ_2. Curves are Gaussian fits to the data. Dashed lines are mean values. (D) Illustration of the large degree of twist in a crenactin dimer. (E) The dihedral angle (φ) of the bottom subunit in a crenactin-ATP dimer was highly correlated with dimer twist in unconstrained simulations. (F) Steering the dihedral angle of the bottom subunit of a crenactin-ATP dimer from 22.6˚ to 26.7˚ caused a systematic shift in dimer twist. Curves are Gaussian fits to the data. Dashed lines are mean values.

https://doi.org/10.1371/journal.pcbi.1006683.g005

Discussion

Through all-atom MD simulations of four actin-family proteins, we identified both conserved and specific dynamical behaviors across the actin family. First, we confirmed that the dihedral and opening angles between the centers-of-mass of the four subdomains represent the majority of conformational changes. In all simulated prokaryotic actins, the four subdomains exhibited high stability throughout the simulation, even as the whole protein changed conformation (Figs 2E, 4B, S2 and S8C). This analysis supports the model used by previous MD studies that measured dihedral and opening angles of actins [4, 13, 32], and provides a verified metric for future MD simulations of actin-family proteins.

Based on our findings, we propose a general model of the regulation of the structure of actin-family filaments in which the intra-subunit dihedral or opening angle of an actin monomer regulates filament bending and/or twisting angles. The model suggests a mechanistic explanation for previous experimental results that have revealed variable filament structures for actin homologs. Electron microscopy of MreB, for instance, revealed straight filaments and arc-like filaments [6, 8], and cryo-EM of crenactin filaments showed highly variable twists

ranging from 32˚ to 56˚ [35]. Our simulations suggest that changes to bound-nucleotide state explain some of the variability in bend and twist for these dimers by tuning the dihedral angles of each subunit, highlighting a conserved mechanism by which actin homologs can adopt a range of filament conformations.

Additionally, our finding that dihedral angle changes drive bending in FtsA and MreB but twisting in crenactin (Figs 5 and S7) indicate that the mechanism is not a trivial mechanical consequence of the four-subdomain structure of actin homologs. Instead, the coupling between dihedral angle and key filament angles has likely been tuned for alternative filament behaviors over evolutionary time scales. For actin, previous studies have shown that its double-protofilament, helical structure leads to twist-bend coupling, as the double-protofilament interface constrains the allowed conformational space [36]. Similar behaviors are likely in the recently identified double-protofilament conformation of *Caulobacter crescentus* MreB [15], for which our simulations suggest that the nucleotide-dependent bending in single protofilaments would be translated to nucleotide-dependent twisting of double protofilaments due to conformational constraints. For filaments such as crenactin that exhibit substantial twisting, the twisting can couple strongly to bending through membrane binding [37], through balancing between the favorable energies of membrane binding and the required energy cost of untwisting the polymer along the membrane surface to expose the membrane-binding interface. Filament bending and twisting can thus be regulated by many interacting factors, calling for simulations of larger biomolecular systems and longer simulation times. Longer and more replicate simulations can also provide more information about the degree to which states truly represent an equilibrium, as opposed to transitions between multiple states. In cases where simulations are currently prohibitive for all-atom MD simulations, course-grained models similar to those previously utilized for actin may prove informative [38].

We observed distinct behaviors across actin homologs in terms of nucleotide dependence that may provide insight regarding the biochemical activities of each protein. MreB and ParM monomers exhibited distinct nucleotide-dependent states (Figs 2A–2D and 4A). These monomers have been shown to have ATPase activity [21, 39], suggesting that structural changes occur during the hydrolysis of ATP. Our results are also synergistic with efforts to translate the conformational variability of bacterial actin homologs for engineered purposes, including using ParM as a biosensor for ADP [40]. Numerous studies have attempted to detect ATPase activity in FtsA, but have found little or no activity [22, 41, 42]. Our simulations visualized distinct and reproducible nucleotide-dependent states (Fig 3), albeit with smaller differences than MreB or ParM. Similar to our previous observation that the bending axis of an FtsA dimer rapidly changes upon release from crystal contacts [17], there is likely flexibility in the conformation of FtsA subunits that is masked in X-ray crystallography by symmetry requirements. For crenactin, we did not observe nucleotide dependence in monomer conformation in our simulations, all of which were carried out at 37˚C (S8 Fig). Crenactin has little ATPase activity at 37˚C, with maximum ATPase activity at 90˚C, which is far outside the temperature range for simulations with CHARMM force fields [12]. Thus, it remains to be seen whether crenactin behaves more like MreB/ParM or FtsA in its native environmental conditions of thermophilic temperatures. Hsp70, which forms a superfamily with actin based on a common fold, also exhibits nucleotide-dependent allostery [43], indicating that these intramonomeric changes may be general to a larger group of proteins. This basis for the large intramonomeric conformational changes in proteins such as MreB and ParM also suggests a strategy for the future design of proteins with similar flexibility and for the design of antibiotics that inhibit or disrupt these motions.

For prokaryotic actins, small perturbations in the protein's environment can vastly impact structure. Many prokaryotic actins require binding proteins to confer their function *in vivo*,

such as RodZ binding to MreB [44, 45]. Furthermore, simulations of FtsA-FtsZ complexes could reveal why cell division relies upon the correct ratio of FtsA and FtsZ [46]. Crystal structures of FtsA-FtsZ complexes exist, but as we have shown with FtsA, crystal structures do not necessarily capture the relevant physiological state [5], motivating the use of complementary techniques such as MD. In addition, genetic perturbations to prokaryotic actins can significantly impact cellular phenotypes. For example, mutations in MreB can have large effects on cell size and shape as well as MreB's ability to sense curvature [47, 48]. Certain ParM mutations restrict the formation of helical filaments [49], and a variety of FtsA mutations restore viability after *zipA* deletion and alter cell shape [50–52]. Ultimately, crystallography, cryo-EM, *in vivo* light microscopy, and MD should prove a powerful combination for understanding and exploiting the numerous functions of cytoskeletal proteins.

Methods

MD simulations

All simulations (S1 Table) were performed using the molecular dynamics package NAMD v. 2.10 [53] with the CHARMM36 force field [31], except where otherwise noted, including CMAP corrections [54]. Water molecules were described with the TIP3P model [55]. Long-range electrostatic forces were evaluated by means of the particle-mesh Ewald summation approach with a grid spacing of <1 Å. An integration time step of 2 fs was used [56]. Bonded terms and short-range, non-bonded terms were evaluated every time step, and long-range electrostatics were evaluated every other time step. Constant temperature ($T = 310$ K) was maintained using Langevin dynamics [57], with a damping coefficient of 1.0 ps^{-1}. A constant pressure of 1 atm was enforced using the Langevin piston algorithm [58] with a decay period of 200 fs and a time constant of 50 fs. Setup, analysis, and rendering of the simulation systems were performed with the software VMD v. 1.9.2 [59]. Steering of the dihedral angle and of distances between residues was achieved by introducing collective forces to constrain angles and distances to defined values through the collective variable functionality of NAMD [53].

Simulated systems

MD simulations performed in this study are described in S1 Table. For simulated systems initialized from a MreB crystal structure, the crystallographic structure of *T. maratima* MreB bound to AMP-PMP (PDB ID: 1JCG) [4] was used; for FtsA, the crystallographic structure of *T. maratima* FtsA bound to ATP gamma A (PDB ID: 4A2B) [5] was used; for ParM, the crystallographic structure of *E. coli* ParM (PDB ID: 1MWM) [6] bound to ADP was used; for crenactin, the crystallographic structure of *P. calidifontis* crenactin bound to ADP (PDB ID: 4CJ7) [12] was used. The bound nucleotide was replaced by both ATP and ADP for all simulated systems, and Mg^{2+}-chelating ions were added for stability. Water and neutralizing ions were added around each monomer or dimer, resulting in final simulation sizes of up to 157,000 atoms. All unconstrained simulations were run for 58–220 ns. All steered simulations were run until equilibrium was reached. For mean values and distributions of measurements, unless otherwise noted, only the last 30 ns of unconstrained simulations or the last 20 ns of steered simulations were used. To test whether simulations had potentially reached equilibrium, measurement distributions were fit to a Gaussian, and mean values were compared across replicates.

Analysis of dihedral and opening angles

The centers-of-mass of the four subdomains of each protein were obtained using VMD. For each time step, we calculated one opening angle from the dot product between the vector

defined by the centers-of-mass of subdomains IIA and IIB and the vector defined by the centers-of-mass of subdomains IIA and IA. Similarly, we calculated a second opening angle from the dot products between the vectors defined by the centers-of-mass of subdomains IA and IB (or IA and IC for FtsA) and of subdomains IA and IIA. The opening angles we report are the average of these two opening angles. The dihedral angle was defined as the angle between the vector normal to a plane defined by subdomains IA, IB, and IIA and the vector normal to a plane defined by subdomains IIB, IIA, and IA. Subdomain definitions were obtained by mapping the boundaries based on a structure-based sequence alignment with eukaryotic actin, and are provided for each protein in S2 Table.

Analysis of bending and twisting angles

At each time step of a dimer simulation, the coordinate system of the bottom and top monomers was defined using three unit vectors $\{\mathbf{d_1}, \mathbf{d_2}, \mathbf{d_3}\}$. $\mathbf{d_1}$ approximately aligns to the center-of-mass between the two subunits, and bending around $\mathbf{d_3}$ is defined to be zero at the start of the simulation. Rotation around $\mathbf{d_1}$ represents twist between the bottom and top subunits. Since $\mathbf{d_3}$ is defined to be zero at the start of the simulation, $\mathbf{d_2}$ represents the ideal bending axis. $\mathbf{d_3}$ represents bending in a direction orthogonal to $\mathbf{d_2}$.

Linear regression

Linear regressions were performed using the LinearModel class in Matlab. The reported *p*-values of linear regressions are for the *F*-statistic, where the null hypothesis is a zero coefficient of regression. To take into account typical correlation time scales, *p*-values were adjusted to represent a sample size corresponding to a 1-ns or 3-ns interval between independent states in the simulation [60].

Supporting information

S1 Fig. Opening angle trajectories of MreB monomers. A) In CHARMM36 simulations, an ATP-bound MreB monomer adopted larger opening angles than the value in the crystal structure (dashed line).
B) The trajectory of the opening angles of a MreB-ATP monomer simulation using CHARMM36 force fields shows that ATP-bound MreB stabilized with a larger opening angle than ADP-bound MreB.
C) The trajectory of the dihedral angle of an MreB-ATP monomer simulation using CHARMM36 force fields shows that ATP-bound MreB stabilized with a larger dihedral angle than ADP-bound MreB. This finding is consistent with results reported using CHARMM27 force fields.
D) The trajectory of the RMSD values of an MreB-ATP monomer in a CHARMM27 simulation relative to the initial equilibrated structure exhibited large changes as the protein adopted an open conformation (black line). Nonetheless, the RMSDs of the four subdomains remained ~2 Å, indicating that conformational dynamics were small within each subdomain.
E) RMSD trajectories of the CHARMM27 simulation relative to the endpoint of the CHARMM36 MreB-ATP-1 simulation as the reference displayed differences in structure at the protein level. Nevertheless, the subdomains remained structurally similar.
F) PCA on the trajectory of the entire protein, and separately on the trajectories of each subdomain, of an ATP-bound MreB monomer. The eigenvector with the largest eigenvalue explained 70.3% of the variance in the entire protein, versus 25.5% to 45.9% of the variance in the subdomains. The eigenvectors with the 10 largest eigenvalues collectively explained 92.2% of the variance in the entire protein, versus 78.0% to 80.6% of the variance in the subdomains.

G) The locations of C_α atoms in MreB in conformations corresponding to the mean structure plus the eigenvector with the largest eigenvalue of the trajectory of an unconstrained simulation of an ATP-bound monomer, scaled by *s*. Conformational changes associated with movement along that eigenvector correspond to changes in the opening angle.
H) Bio3D cross-correlation analysis of an ATP-bound MreB monomer shows that the trajectories of residues within IA/IIA were correlated, as were those in IB/IIB, while the trajectories of IA/IIA were opposite from IB/IIB.
(TIF)

S2 Fig. Subunit RMSD of FtsA monomers. The trajectory of the RMSD values of an FtsA-ATP monomer simulation relative to the initial equilibrated structure exhibited small changes throughout the simulation (black line). Similarly, the RMSDs of the subunits of FtsA were also small.
(TIF)

S3 Fig. Steered FtsA monomer simulations. A) Trajectory of the opening angle of a steered ATP-bound FtsA monomer. The FtsA monomer was steered up to 112˚. Upon release, the opening angle of the monomer stabilized at 110˚, indicating that the opening angle of the ATP-bound state is stable to perturbations.
B) Trajectory of the opening angle of a steered ADP-bound FtsA monomer. The FtsA monomer was steered down to 108˚. Upon release, the opening angle of the monomer stabilized at 112˚, indicating that the opening angle of the ADP-bound state is stable to perturbations.
(TIF)

S4 Fig. ParM monomer opening and dihedral angle. The dihedral angle (A) and opening angle (B) trajectories for two ATP-bound and two ADP-bound ParM simulations are shown. ParM dihedral angle did not display strong nucleotide dependence across replicate monomer simulations.
(TIF)

S5 Fig. ParM opening without high RMSF residues. Removing high RMSF residues in ParM did not affect the nucleotide dependence of the opening angle of ParM monomers.
(TIF)

S6 Fig. Unconstrained ParM interactions. Interactions between residues 58–67 and 173–174 persisted throughout the ParM-ATP-2 (A) and ParM-ATP-3 (B) simulations, which opened much less than ParM-ATP-1, the simulation in which these interactions were disrupted (Fig 4E).
(TIF)

S7 Fig. Steered dihedral angle in MreB dimers. We observed an inverse relationship between the dihedral angle of the bottom subunit and filament bending in MreB dimer simulations. Dashed lines show mean values.
(TIF)

S8 Fig. Crenactin monomer simulations. A-B) The dihedral angle (A) and opening angle (B) trajectories for two ATP-bound and two ADP-bound crenactin simulations are shown. The trajectories indicate little nucleotide dependence in monomer conformation.
C) The trajectory of the RMSD values of a crenactin-ATP monomer simulation relative to the initial equilibrated structure exhibited small changes throughout the simulation (black line). Similarly, the RMSDs of the subunits of crenactin were also small.
(TIF)

S9 Fig. FtsA and crenactin dimer trajectories. A-C) Trajectories of twisting and two bending angles for two replicate simulations each of ATP- and ADP-bound FtsA dimers.
D-F) Trajectories of twisting and two bending angles for two replicate simulations each of ATP- and ADP-bound crenactin dimers.
(TIF)

S10 Fig. Steered dihedral trajectories for FtsA and crenactin. A) Trajectories of the dihedral angle of the bottom subunit in FtsA dimers in which the dihedral angle was steered to 16.4˚, 20.8˚, 25.5˚, and 29.6˚.
B) Trajectories of the dihedral angle of the bottom subunit in crenactin dimers in which the dihedral angle was steered to 22.6˚, 23.4˚, and 26.7˚.
(TIF)

S1 Table. MD simulations in this study. All unconstrained simulations were replicated at least twice, with their simulation times indicated in separate rows.
(DOCX)

S2 Table. Subdomain definitions by residue numbers.
(DOCX)

Acknowledgments

We thank Jen Hsin, Jan Löwe, and the Huang lab for helpful discussions.

Author Contributions

Conceptualization: Natalie Ng, Alexandre Colavin, Kerwyn Casey Huang.

Data curation: Natalie Ng, Handuo Shi, Kerwyn Casey Huang.

Formal analysis: Natalie Ng, Handuo Shi, Kerwyn Casey Huang.

Funding acquisition: Handuo Shi, Alexandre Colavin, Kerwyn Casey Huang.

Investigation: Natalie Ng, Handuo Shi, Kerwyn Casey Huang.

Methodology: Natalie Ng, Handuo Shi, Kerwyn Casey Huang.

Project administration: Handuo Shi, Kerwyn Casey Huang.

Resources: Natalie Ng, Handuo Shi, Kerwyn Casey Huang.

Software: Natalie Ng, Handuo Shi.

Supervision: Handuo Shi, Alexandre Colavin, Kerwyn Casey Huang.

Validation: Natalie Ng, Handuo Shi, Kerwyn Casey Huang.

Visualization: Natalie Ng, Kerwyn Casey Huang.

Writing – original draft: Natalie Ng, Handuo Shi, Kerwyn Casey Huang.

Writing – review & editing: Natalie Ng, Handuo Shi, Alexandre Colavin, Kerwyn Casey Huang.

References

1. Fletcher DA, Mullins RD. Cell mechanics and the cytoskeleton. Nature. 2010; 463(7280):485–92. https://doi.org/10.1038/nature08908 PMID: 20110992

2. Shih YL, Rothfield L. The bacterial cytoskeleton. Microbiol Mol Biol Rev. 2006; 70(3):729–54. https://doi.org/10.1128/MMBR.00017-06 PMID: 16959967
3. Izore T, Duman R, Kureisaite-Ciziene D, Lowe J. Crenactin from *Pyrobaculum calidifontis* is closely related to actin in structure and forms steep helical filaments. FEBS Lett. 2014; 588(5):776–82. https://doi.org/10.1016/j.febslet.2014.01.029 PMID: 24486010
4. van den Ent F, Amos LA, Lowe J. Prokaryotic origin of the actin cytoskeleton. Nature. 2001; 413 (6851):39–44. https://doi.org/10.1038/35092500 PMID: 11544518
5. van den Ent F, Löwe J. Crystal structure of the cell division protein FtsA from *Thermotoga maritima*. The EMBO Journal. 2000; 19(20):5300–7. https://doi.org/10.1093/emboj/19.20.5300 PMID: 11032797
6. van den Ent F, Moller-Jensen J, Amos LA, Gerdes K, Lowe J. F-actin-like filaments formed by plasmid segregation protein ParM. EMBO J. 2002; 21(24):6935–43. https://doi.org/10.1093/emboj/cdf672 PMID: 12486014
7. Kabsch W, Holmes KC. The actin fold. FASEB J. 1995; 9(2):167–74. PMID: 7781919
8. Esue O, Cordero M, Wirtz D, Tseng Y. The assembly of MreB, a prokaryotic homolog of actin. J Biol Chem. 2005; 280(4):2628–35. https://doi.org/10.1074/jbc.M410298200 PMID: 15548516
9. Shaevitz JW, Gitai Z. The structure and function of bacterial actin homologs. Cold Spring Harb Perspect Biol. 2010; 2(9):a000364. https://doi.org/10.1101/cshperspect.a000364 PMID: 20630996
10. Pichoff S, Lutkenhaus J. Unique and overlapping roles for ZipA and FtsA in septal ring assembly in *Escherichia coli*. EMBO J. 2002; 21(4):685–93. https://doi.org/10.1093/emboj/21.4.685 PMID: 11847116
11. Jensen RB, Gerdes K. Mechanism of DNA segregation in prokaryotes: ParM partitioning protein of plasmid R1 co-localizes with its replicon during the cell cycle. EMBO J. 1999; 18(14):4076–84. https://doi.org/10.1093/emboj/18.14.4076 PMID: 10406812
12. Ettema TJ, Lindas AC, Bernander R. An actin-based cytoskeleton in archaea. Mol Microbiol. 2011; 80 (4):1052–61. https://doi.org/10.1111/j.1365-2958.2011.07635.x PMID: 21414041
13. Colavin A, Hsin J, Huang KC. Effects of polymerization and nucleotide identity on the conformational dynamics of the bacterial actin homolog MreB. Proceedings of the National Academy of Sciences. 2014; 111(9):3585–90.
14. Polka JK, Kollman JM, Agard DA, Mullins RD. The structure and assembly dynamics of plasmid actin AlfA imply a novel mechanism of DNA segregation. J Bacteriol. 2009; 191(20):6219–30. https://doi.org/10.1128/JB.00676-09 PMID: 19666709
15. van den Ent F, Izore T, Bharat TA, Johnson CM, Lowe J. Bacterial actin MreB forms antiparallel double filaments. Elife. 2014; 3:e02634. https://doi.org/10.7554/eLife.02634 PMID: 24843005
16. Jones LJ, Carballido-Lopez R, Errington J. Control of cell shape in bacteria: helical, actin-like filaments in *Bacillus subtilis*. Cell. 2001; 104(6):913–22. PMID: 11290328
17. Hsin J, Fu R, Huang KC. Dimer dynamics and filament organization of the bacterial cell division protein FtsA. J Mol Biol. 2013; 425(22):4415–26. https://doi.org/10.1016/j.jmb.2013.07.016 PMID: 23871894
18. Bharat TA, Murshudov GN, Sachse C, Lowe J. Structures of actin-like ParM filaments show architecture of plasmid-segregating spindles. Nature. 2015; 523(7558):106–10. https://doi.org/10.1038/nature14356 PMID: 25915019
19. Bergeron JR, Hutto R, Ozyamak E, Hom N, Hansen J, Draper O, et al. Structure of the magnetosome-associated actin-like MamK filament at subnanometer resolution. Protein Sci. 2017; 26(1):93–102. https://doi.org/10.1002/pro.2979 PMID: 27391173
20. Galkin VE, Orlova A, Rivera C, Mullins RD, Egelman EH. Structural polymorphism of the ParM filament and dynamic instability. Structure. 2009; 17(9):1253–64. https://doi.org/10.1016/j.str.2009.07.008 PMID: 19748346
21. Esue O, Wirtz D, Tseng Y. GTPase activity, structure, and mechanical properties of filaments assembled from bacterial cytoskeleton protein MreB. J Bacteriol. 2006; 188(3):968–76. https://doi.org/10.1128/JB.188.3.968-976.2006 PMID: 16428401
22. Loose M, Mitchison TJ. The bacterial cell division proteins FtsA and FtsZ self-organize into dynamic cytoskeletal patterns. Nat Cell Biol. 2014; 16(1):38–46. https://doi.org/10.1038/ncb2885 PMID: 24316672
23. Erickson HP. Modeling the physics of FtsZ assembly and force generation. Proc Natl Acad Sci U S A. 2009; 106(23):9238–43. https://doi.org/10.1073/pnas.0902258106 PMID: 19478069
24. Erickson HP. FtsZ, a tubulin homologue in prokaryote cell division. Trends Cell Biol. 1997; 7(9):362–7. https://doi.org/10.1016/S0962-8924(97)01108-2 PMID: 17708981

25. Erickson HP, Taylor DW, Taylor KA, Bramhill D. Bacterial cell division protein FtsZ assembles into protofilament sheets and minirings, structural homologs of tubulin polymers. Proc Natl Acad Sci U S A. 1996; 93(1):519–23. PMID: 8552673

26. Zheng X, Diraviyam K, Sept D. Nucleotide effects on the structure and dynamics of actin. Biophys J. 2007; 93(4):1277–83. https://doi.org/10.1529/biophysj.107.109215 PMID: 17526584

27. Chu JW, Voth GA. Allostery of actin filaments: molecular dynamics simulations and coarse-grained analysis. Proc Natl Acad Sci U S A. 2005; 102(37):13111–6. https://doi.org/10.1073/pnas.0503732102 PMID: 16135566

28. Hsin J, Gopinathan A, Huang KC. Nucleotide-dependent conformations of FtsZ dimers and force generation observed through molecular dynamics simulations. Proc Natl Acad Sci U S A. 2012; 109 (24):9432–7. https://doi.org/10.1073/pnas.1120761109 PMID: 22647609

29. Li Y, Hsin J, Zhao L, Cheng Y, Shang W, Huang KC, et al. FtsZ protofilaments use a hinge-opening mechanism for constrictive force generation. Science. 2013; 341(6144):392–5. https://doi.org/10.1126/science.1239248 PMID: 23888039

30. Martín-García F, Papaleo E, Gomez-Puertas P, Boomsma W, Lindorff-Larsen K. Comparing Molecular Dynamics Force Fields in the Essential Subspace. PLoS ONE. 2015; 10(3):e0121114. https://doi.org/10.1371/journal.pone.0121114 PMID: 25811178

31. Best RB, Zhu X, Shim J, Lopes PE, Mittal J, Feig M, et al. Optimization of the additive CHARMM all-atom protein force field targeting improved sampling of the backbone phi, psi and side-chain chi(1) and chi(2) dihedral angles. J Chem Theory Comput. 2012; 8(9):3257–73. https://doi.org/10.1021/ct300400x PMID: 23341755

32. Pfaendtner J, Lyman E, Pollard TD, Voth GA. Structure and Dynamics of the Actin Filament. Journal of Molecular Biology. 2010; 396(2):252–63. https://doi.org/10.1016/j.jmb.2009.11.034 PMID: 19931282

33. Grant BJ, Rodrigues AP, ElSawy KM, McCammon JA, Caves LS. Bio3d: an R package for the comparative analysis of protein structures. Bioinformatics. 2006; 22(21):2695–6. https://doi.org/10.1093/bioinformatics/btl461 PMID: 16940322

34. Gayathri P, Fujii T, Namba K, Lowe J. Structure of the ParM filament at 8.5A resolution. J Struct Biol. 2013; 184(1):33–42. https://doi.org/10.1016/j.jsb.2013.02.010 PMID: 23462100

35. Braun T, Orlova A, Valegard K, Lindas AC, Schroder GF, Egelman EH. Archaeal actin from a hyperthermophile forms a single-stranded filament. Proc Natl Acad Sci U S A. 2015; 112(30):9340–5. https://doi.org/10.1073/pnas.1509069112 PMID: 26124094

36. Enrique M, Roland J, McCullough BR, Blanchoin L, Martiel J-L. Origin of twist-bend coupling in actin filaments. Biophysical journal. 2010; 99(6):1852–60. https://doi.org/10.1016/j.bpj.2010.07.009 PMID: 20858430

37. Quint DA, Gopinathan A, Grason GM. Shape selection of surface-bound helical filaments: biopolymers on curved membranes. Biophysical journal. 2016; 111(7):1575–85. https://doi.org/10.1016/j.bpj.2016.08.017 PMID: 27705779

38. Chu J-W, Voth GA. Allostery of actin filaments: molecular dynamics simulations and coarse-grained analysis. Proceedings of the National Academy of Sciences. 2005; 102(37):13111–6.

39. Jensen RB, Gerdes K. Partitioning of plasmid R1. The ParM protein exhibits ATPase activity and interacts with the centromere-like ParR-parC complex. J Mol Biol. 1997; 269(4):505–13. https://doi.org/10.1006/jmbi.1997.1061 PMID: 9217256

40. Kunzelmann S, Webb MR. A fluorescent, reagentless biosensor for ADP based on tetramethylrhodamine-labeled ParM. ACS Chem Biol. 2010; 5(4):415–25. https://doi.org/10.1021/cb9003173 PMID: 20158267

41. Beuria TK, Mullapudi S, Mileykovskaya E, Sadasivam M, Dowhan W, Margolin W. Adenine nucleotide-dependent regulation of assembly of bacterial tubulin-like FtsZ by a hypermorph of bacterial actin-like FtsA. J Biol Chem. 2009; 284(21):14079–86. https://doi.org/10.1074/jbc.M808872200 PMID: 19297332

42. Szwedziak P, Wang Q, Freund SM, Lowe J. FtsA forms actin-like protofilaments. EMBO J. 2012; 31 (10):2249–60. https://doi.org/10.1038/emboj.2012.76 PMID: 22473211

43. English CA, Sherman W, Meng W, Gierasch LM. The Hsp70 interdomain linker is a dynamic switch that enables allosteric communication between two structured domains. J Biol Chem. 2017; 292 (36):14765–74. https://doi.org/10.1074/jbc.M117.789313 PMID: 28754691

44. Morgenstein RM, Bratton BP, Nguyen JP, Ouzounov N, Shaevitz JW, Gitai Z. RodZ links MreB to cell wall synthesis to mediate MreB rotation and robust morphogenesis. Proc Natl Acad Sci U S A. 2015; 112(40):12510–5. https://doi.org/10.1073/pnas.1509610112 PMID: 26396257

45. Bendezu FO, Hale CA, Bernhardt TG, de Boer PA. RodZ (YfgA) is required for proper assembly of the MreB actin cytoskeleton and cell shape in *E. coli*. EMBO J. 2009; 28(3):193–204. https://doi.org/10.1038/emboj.2008.264 PMID: 19078962

46. Dai K, Lutkenhaus J. The proper ratio of FtsZ to FtsA is required for cell division to occur in *Escherichia coli*. J Bacteriol. 1992; 174(19):6145–51. PMID: 1400163

47. Dye NA, Pincus Z, Fisher IC, Shapiro L, Theriot JA. Mutations in the nucleotide binding pocket of MreB can alter cell curvature and polar morphology in *Caulobacter*. Mol Microbiol. 2011; 81(2):368–94. https://doi.org/10.1111/j.1365-2958.2011.07698.x PMID: 21564339

48. Shi H, Colavin A, Bigos M, Tropini C, Monds RD, Huang KC. Deep phenotypic mapping of bacterial cytoskeletal mutants reveals physiological robustness to cell size. Current Biology. 2017.

49. Popp D, Iwasa M, Maeda K, Narita A, Oda T, Maeda Y. Protofilament formation of ParM mutants. J Mol Biol. 2009; 388(2):209–17. https://doi.org/10.1016/j.jmb.2009.02.057 PMID: 19265709

50. Pichoff S, Shen B, Sullivan B, Lutkenhaus J. FtsA mutants impaired for self-interaction bypass ZipA suggesting a model in which FtsA's self-interaction competes with its ability to recruit downstream division proteins. Mol Microbiol. 2012; 83(1):151–67. https://doi.org/10.1111/j.1365-2958.2011.07923.x PMID: 22111832

51. Geissler B, Elraheb D, Margolin W. A gain-of-function mutation in *ftsA* bypasses the requirement for the essential cell division gene *zipA* in *Escherichia coli*. Proc Natl Acad Sci U S A. 2003; 100(7):4197–202. https://doi.org/10.1073/pnas.0635003100 PMID: 12634424

52. Gayda RC, Henk MC, Leong D. C-shaped cells caused by expression of an *ftsA* mutation in *Escherichia coli*. J Bacteriol. 1992; 174(16):5362–70. PMID: 1644763

53. Phillips JC, Braun R, Wang W, Gumbart J, Tajkhorshid E, Villa E, et al. Scalable molecular dynamics with NAMD. J Comput Chem. 2005; 26(16):1781–802. https://doi.org/10.1002/jcc.20289 PMID: 16222654

54. Mackerell AD Jr., Feig M, Brooks CL 3rd. Extending the treatment of backbone energetics in protein force fields: limitations of gas-phase quantum mechanics in reproducing protein conformational distributions in molecular dynamics simulations. J Comput Chem. 2004; 25(11):1400–15. https://doi.org/10.1002/jcc.20065 PMID: 15185334

55. Jorgensen JH, Johnson JE, Alexander GA, Paxson R, Alderson GL. Comparison of automated and rapid manual methods for the same-day identification of Enterobacteriaceae. Am J Clin Pathol. 1983; 79(6):683–7. PMID: 6342361

56. Tuckerman M, Berne BJ, Martyna GJ. Reversible multiple time scale molecular dynamics. J Chem Phys. 1992; 97(3):1990–2001.

57. Brünger A, Brooks CL, Karplus M. Stochastic boundary conditions for molecular dynamics simulations of ST2 water. Chem Phys Lett. 1984; 105(5):495–500.

58. Feller SE, Zhang Y, Pastor RW, Brooks BR. Constant pressure molecular dynamics simulation: the Langevin piston method. J Chem Phys. 1995; 103(11):4613–21.

59. Humphrey W, Dalke A, Schulten K. VMD: visual molecular dynamics. J Mol Graph. 1996; 14(1):33–8, 27–8. PMID: 8744570

60. Lyman E, Zuckerman DM. On the structural convergence of biomolecular simulations by determination of the effective sample size. J Phys Chem B. 2007; 111(44):12876–82. https://doi.org/10.1021/jp073061t PMID: 17935314